Research Square

Preprints are preliminary reports that have not undergone peer review.
They should not be considered conclusive, used to inform clinical practice,
or referenced by the media as validated information.

# Optimization of CISSe/CdS/ZnO/SLG Solar Cell: Simulation Study on Electrical losses Effected by Metastable Defects

**Mouad Chettab**

mouad.chettab@doc.umc.edu.dz

Université de Frères Mentouri Constantine 01

**Selma Rabhi**

Constantine 01 University

**Halima Djaaboube**

Université de Frères Mentouri Constantine 01

**Research Article**

**Keywords:** CISSe, Thin films, Illumination, SCAPS, Solar cells, Photovoltaic parameters. Metastable defects

**Posted Date:** June 26th, 2026

**DOI:** https://doi.org/10.21203/rs.3.rs-9873482/v1

**License:** This work is licensed under a Creative Commons Attribution 4.0 International License.
Read Full License

**Additional Declarations:** No competing interests reported.

# Optimization of CISSe/CdS/ZnO/SLG Solar Cell: Simulation Study on Electrical losses Effected by Metastable Defects.

**Mouad Chettab[1*], Selma Rabhi[2] and Halima Djaaboube[1]**

[1]Thin films and interfaces laboratory, Université de Frères Mentouri Constantine 01, Constantine, Algérie.

[2] Laboratory of Innovative Environmental Preservation Techniques, Department of Chemistry, Constantine 01 University, 25000 Constantine, Algeria.

Correspondant author* : **mouad.chettab@doc.umc.edu.dz**

**Abstract**

The performance of (CISSe) thin-film solar cells is strongly influenced by interfacial band alignment, contact properties, and carrier-transport mechanisms. In this work, a comprehensive numerical investigation of CISSe/CdS/ZnO/SLG solar cells was carried out using SCAPS-1D to evaluate the combined effects of illumination direction, back-contact metal work function, parasitic resistances, electron affinity, and absorber bandgap on device performance. The results reveal that the conventional top-illuminated configuration outperforms bottom illumination, achieving a power conversion efficiency (PCE) of 22.10%, a fill factor (FF) of 80.31%, an open-circuit voltage (Voc) of 0.5775 V, and a short-circuit current density (Jsc) of 47.20 mA $cm^{-2}$. Band-alignment analysis shows that a cliff-like conduction-band offset of -0.2 eV at the CdS/CISSe interface and a large valence-band barrier of -0.9 eV at the ZnO/CdS interface contribute to carrier accumulation and recombination losses. Furthermore, increasing the back-contact metal work function from 4.9 to 5.7 eV reduces the majority-carrier barrier height from 0.44 to -0.36 eV, promoting quasi-Ohmic contact formation and improving carrier extraction. The effects of series and shunt resistances demonstrate that low Rs (2 $\Omega \cdot cm^2$) and high Rsh (10 $k\Omega \cdot cm^2$) are essential for minimizing electrical losses and maximizing photovoltaic performance. In addition, absorber-layer engineering through simultaneous optimization of electron affinity and bandgap significantly enhances device operation. The optimum configuration, obtained at $\chi$ = 4.05 eV and Eg = 1.45 eV, delivers a maximum PCE of 33.34%, FF of 85.05%, Voc of 0.9115 V, and Jsc of 44.27 mA $cm^{-2}$. These findings provide valuable guidelines for the design of next-generation high-performance CISSe thin-film solar cells.

**Keywords:** CISSe, Thin films, Illumination, SCAPS, Solar cells, Photovoltaic parameters. Metastable defects.

## 1. Introduction

Solar energy is considered one of the most important renewable energy sources for meeting current and future global energy needs on a terawatt (TW) scale [1]. Among the different renewable technologies, solar cells are highly effective because they can directly convert sunlight into electrical energy without causing harmful environmental effects [2]. Due to the continuous increase in energy demand around the world, photovoltaic solar power generation has grown rapidly over the last few decades [3]. Recently, Copper indium sulfoselenide (CISSe) thin-film solar cells continue to attract strong scientific interest (figure 01) because of their high absorption coefficient, tunable bandgap [4]. (CISSe) exhibits long-term stability and large effective area [5]. Over the past decade, major research groups-including Ghebouli et al. [6] have repeatedly reported record (CISSe) efficiencies above 30.07 %. In parallel, efficiency progress has been tracked by the National Renewable Energy Laboratory (NREL), which continues to report world-leading results in the CIGS/CISSe category [7]. The photovoltaic performance of solar cells depends not only on the absorber layer but also on the transport layers and interface quality. CdS is widely used as buffer because of their favorable electronic properties, high transparency, and efficient electron extraction ability [8], [9]. Also, ZnO was utilized as TCO material due to its excellent transparence and high mobility [10],[11]. Alongside experimental advancements, numerical device simulation using SCAPS-1D has become essential for analyzing charge transport, recombination mechanisms, and band-alignment effects [12]. A wide range of simulation studies has investigated absorber-layer properties, interface optimization, and back-contact selection for CISSe devices. For instance, many researchers such as Xia et al. [13] and Minemoto et al.[14] have highlighted the critical role of the conduction-band offset (CBO) at the buffer/absorber interface and its direct influence on interface recombination and open-circuit voltage.

Other studies have explored the impact of CdS thickness, front-buffer transparency, and absorber defect density on short-circuit current and fill factor. Specific attention has also been given to the influence of back-contact metal work function. Atowar Rahman et al. [15], for example, demonstrated that increasing the work function of the back metal significantly

enhances charge extraction and boosts device performance. Despite these advances, most existing studies investigate these effects individually-bandgap, electron affinity, $R_s/R_{sh}$, or metal work function without assessing how these factors interact under different illumination conditions. A clear gap remains in understanding how illumination direction, back-contact work function, parasitic resistances, and absorber electronic properties collectively govern CISSe device performance. Very few reports like [16] provide a systematic comparison between top and bottom illumination, even though the illumination pathway strongly influences carrier generation depth, interfacial recombination, and quantum-efficiency behavior. Likewise, while the importance of metal work function is recognized, no study has comprehensively linked work-function tuning with parasitic-resistance effects and absorber-band engineering in a unified simulation framework. The present work addresses these gaps through a detailed SCAPS-1D investigation of CISSe/CdS/ZnO/SLG solar cells.

The novelty of this study lies in three main contributions. First, the effect of illumination direction (top vs. bottom) is analyzed to clarify its role in carrier-generation profiles and recombination pathways. Second, the combined influence of metal work function, series resistance, and shunt resistance is examined to determine their synergistic effects on Voc, Jsc, FF, and efficiency. Third, the study investigates electron-affinity tuning and bandgap engineering of the CISSe absorber to identify optimal band alignment for high-performance operation. Together, these contributions provide an integrated understanding of optical and electrical losses in CISSe devices and offer practical design guidelines for next-generation thin-film.

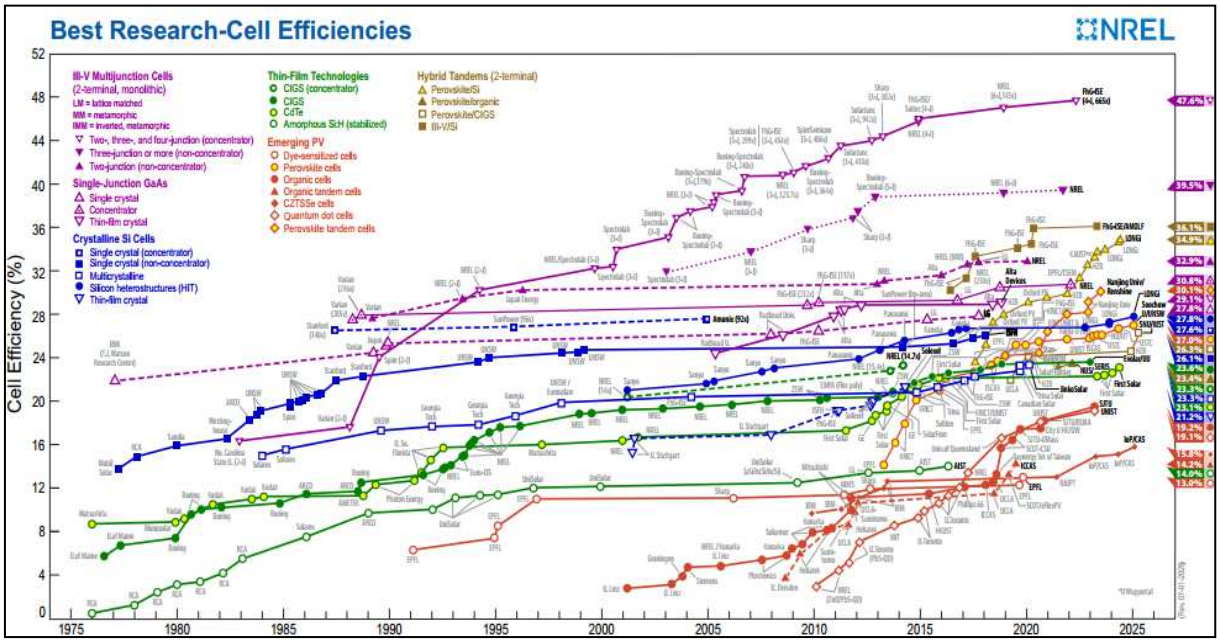



**Figure 01**. Efficiency progress for different solar cells technology between 1975 and 2025 [7].

## 2. Materials and simulation

### 2.1. Materials

The cell model used for this simulation in Figure 01 described the structure of Copper-indium-gallium-selenide (CISSe)-based the based on Pt/CISSe/CdS/ZnO/SLG which consists of transparent conducting oxide (TCO), the absorber layer (CISSe), buffer layer (CdS) and the metal back contact platinum and glass substrate for protection .The cell was illuminated through transparent conductive oxide (TCO), which serves as a window layer. It then passes through the buffer layer (CdS) and eventually enters the absorber layer. The Glass substrate (SLG) was utilized in the aim of

mechanical protection of our solar cell. The figure 02 showed clearly the different layers that formed the device and the depletion zone between the n region and p region.

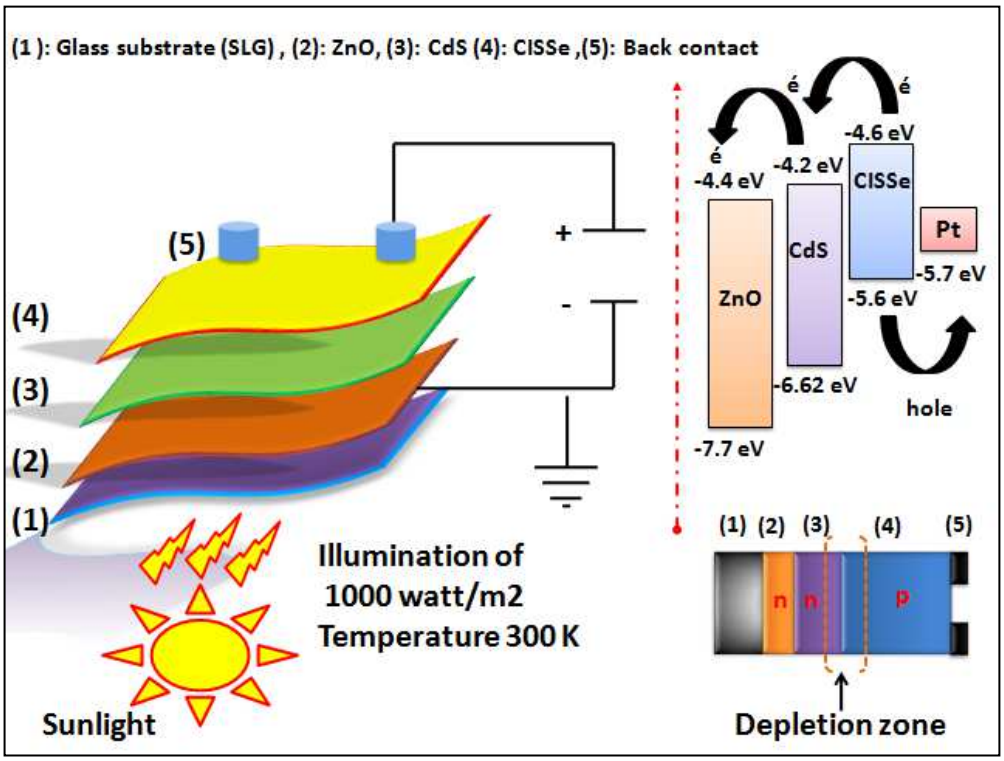



**Figure 02**. Architecture and design of solar cell with the diagram of energy.

### 2.2. Device methodology.

There are several numerical modeling software options accessible to facilitate the computational analysis of photovoltaic cell performance, including SETFOS, SCAPS, SILVACO, COMSOL, and ATLAS [17]. The choice of employing SCAPS-1D version 3.3.10 is driven by its beneficial attributes. SCAPS-1D simulator was developed by Marc Burgelman and his team in 2000, to simulate the electrical characteristics, i.e. simulating alternating current and direct current electrical attributes of thin-film heterojunction solar cells [18]. In 2008, SCAPS was released as an open-source software tool under the GNU General Public License (GPL). This allowed the wider scientific community to access and contributes to the development of SCAPS-1D, this simulator is an one-dimensional solar cell simulation program based on three coupled differential equations by solving the basic semiconductor equations such as the Poisson equation, continuity of electrons and holes [19]. SCAPS analyzes the physics model and explains the recombination profiles, electric field distribution, carrier transport mechanism and individual current densities. Poisson equation can be given by [9],[20]:

$$\frac{\partial^2\psi}{\partial x^2} = \frac{-\partial E}{\partial x} = \frac{\rho}{\epsilon_s} = \frac{-q}{\epsilon_s}\left(p - n + N_d^{+} - N_a^{-} \pm N_{def}\right) \quad \ldots\ldots (1)$$

Where $\psi$ is the electrostatic potential, q is the charge, $\varepsilon$ is the dielectric constant of the medium, p is the free hole density, n is the free electron density, $Nd^{+}$ is the ionized donor density, $Na^{-}$ is the ionized-acceptor density, $n(t)$ and $p(t)$ are trapped electrons density and trapped hole density respectively. The continuity equations of electrons can be described by [21],[22] :

$$-\frac{\partial J_p}{\partial x}+G-U_P(n,p)=0 \quad \text{(2)}$$

$$-\frac{\partial J_n}{\partial x}+G-U_n(n,p)=0 \quad \text{(3)}$$

All the required steps from the definition of layers to the solution of previous equations in order to run the simulation and obtain the photovoltaic parameters were summarized in the figure 03. Also, the configuration of CISSe proprieties and recombination defects parameters were shown in figure 04.

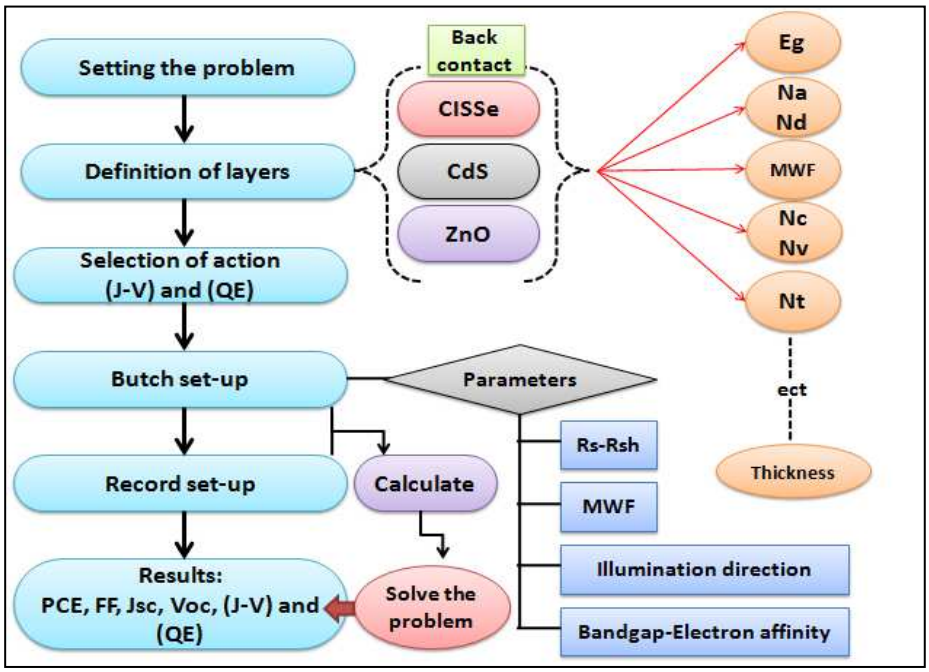



**Figure 03**. Steps for running the simulation code in SCAPS-1D.

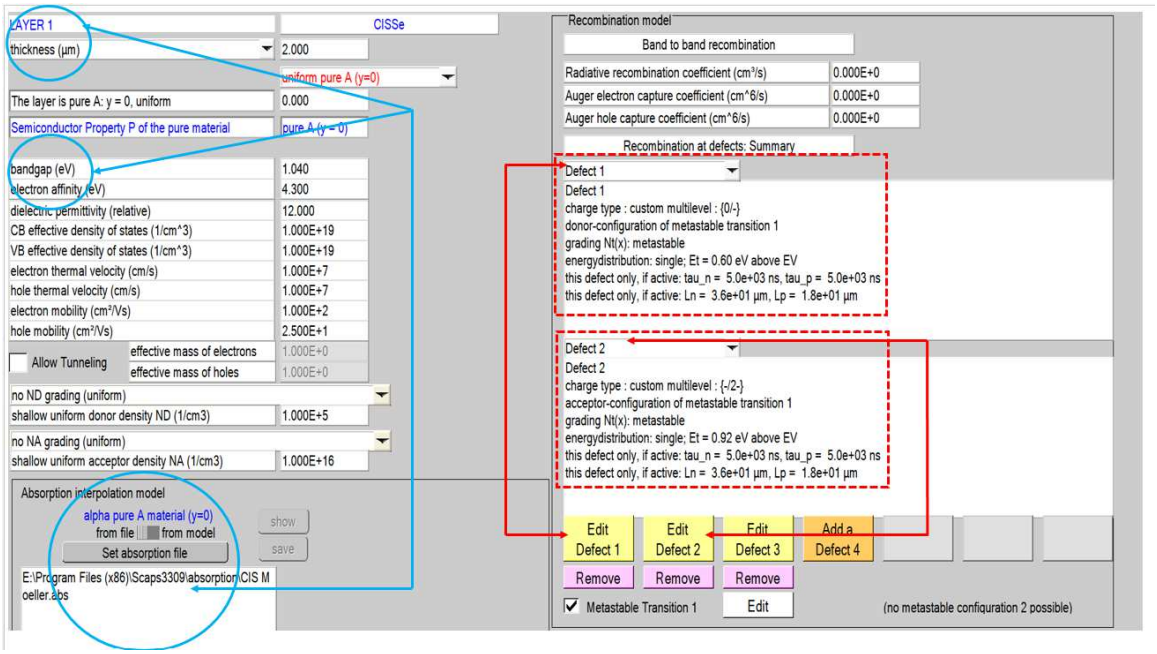



**Figure 04**. Configuration of CISSe proprieties and recombination defects parameters.

**Table 01.** Parameters for ZnO, CdS and CISSe.

| Parameters | p-CISSe | n-CdS | n-ZnO |
|---|---|---|---|
| Thickness (μm) | 2 | 0.1 | 0.2 |
| Band gap (eV) | 1.04 | 2.42 | 3.3 |
| Electron affinity (eV) | 4.3 | 4.1 | 4.1 |
| Dielectric permittivity (relative) | 12 | 10 | 9 |
| CB effective density of states ($cm^{-1}$) | 1.000E+19 | 3.000E+18 | 4.000E+18 |
| VB effective density of states ($cm^{-1}$) | 1.000E+19 | 1.800E+19 | 1.000E+19 |
| Electron thermal velocity (cm/s) | 1.000E+7 | 1.000E+7 | 1.000E+7 |
| Hole thermal velocity (cm/s) | 1.000E+7 | 1.000E+7 | 1.000E+7 |
| Electron mobility ($cm^2/V.s$) | 100 | 100 | 100 |
| Hole mobility ($cm^2/V.s$) | 25 | 25 | 25 |
| Shallow uniform donor density ,$N_D$ ($cm^{-1}$) | 1.000E+5 | 1.000E+17 | 1.000E+18 |
| Shallow uniform donor density ,$N_A$ ($cm^{-1}$) | 1.000E+16 | 0 | 0 |
| Defect density ,$N_t$ (uniform) ($cm^{-3}$) | Metastable | 1.000E+17 | 1.000E+17 |
| References | [4] | [23],[8] | [10],[11]. |

**Table 02.** Energy distribution type of defects with their type of transition.

| Charge type | Custom multilevel |
|---|---|
| Energy distribution (single) | $E_t$ = 0.92 (eV) above $E_v$ |
| Acceptor configuration /transition | Metastable →(CISSe) |

## 3. Results and discussions.

### 3.1. Top/bottom illumination effect

In this subsection, the photovoltaic parameters were calculated with two different type of illumination. First, bottom illumination, means that light enters from the back contact, passing through the absorber layer before reaching buffer /TCO. In contrast, top illumination means that light enters from TCO to CISSe layer. Table 03 showed clearly that the solar cell with top illumination exhibited high efficiency (21.50%) and fill factor (80.31%) while the solar with bottom illumination exhibited moderate efficiency (20.30%) and fill factor (79.70%). The origin of this difference can be understood from the energy-band diagram shown in Figure 5(a).This difference can be attributed to the Conduction and valence band energy between interfaces [24]. According to table 04, the ΔEc cliff (-0.2 eV) at (CdS/CISSe) can cause recombination losses and the large ΔEc (-0.9 eV) at (ZnO/CdS) may trap ($h^+$) which could cause charge accumulation and reducing efficiency [25]. This is because light absorption, charge generation, and carrier transport are highly dependent on the positioning of layers within the device structure [26]. This interpretation is supported by the (J-V) characteristics shown in Figure 5(b), where the top-illuminated device exhibits a slightly improved current-voltage response and higher fill factor. Also, in a conventional top-illuminated solar cell, light first passes through a transparent conductive oxide (TCO) and a buffer layer before reaching the absorber layer, where most of the photon absorption occurs. The penetration depth of light varies with wavelength, as shorter wavelengths (blue light) are absorbed near the surface, while longer wavelengths (red and infrared) penetrate deeper into the absorber. The standard configuration is often optimized to minimize surface recombination and ensuring good band alignment at the interfaces. The transparent front contact should have minimal absorption losses, and the buffer layer should enable efficient charge separation without blocking too much light [27].on the other hand, bottom illumination (or inverted illumination) means that light enters from the back contact, passing through the absorber layer before reaching the buffer and window layers. This can lead to different optical and electrical behaviors. Since the absorber layer is responsible for most of the light absorption, having it directly exposed to incident photons can potentially enhance carrier generation. However,

several challenges arise. First, the back contact may not be optimized for light entry, potentially leading to reflection losses. Second, if the front contact (which is now at the bottom) is not fully transparent, it can block light transmission, reducing the overall short-circuit current (Jsc).Additionally, since charge carriers are generated deeper in the absorber, their collection may be less efficient, especially if recombination rates are high near the back interfaces [16].

**Table 03.** PV parameters with top/bottom illumination effect.

| PV parameters | PCE (%) | FF (%) | Voc (V) | Jsc (mA/cm$^2$) |
|---|---|---|---|---|
| Top illumination | 21.50 | 80.31 | 0.5775 | 47.20 |
| Bottom illumination | 20.30 | 79.70 | 0.5667 | 47.438 |

**Table 04.** Conduction/valence band energy between interfaces.

| **Interfaces** | **ΔEc (eV)** | **ΔEv (eV)** |
|---|---|---|
| **CdS/CISSe** | -0.2 (Cliff) | -0.9 (barrier) |
| **ZnO/CdS** | 0.0 (aligned) | -0.9 (barrier) |

Further insight is obtained from the quantum-efficiency spectra presented in Figure 5(c). Both configurations exhibit high carrier collection in the visible region; however, the top-illuminated structure maintains a higher (QE) over a wider spectral range. The derivative of the (QE) curve reveals a pronounced absorption edge near 0.99 eV, corresponding to the optical bandgap of the CISSe absorber. In addition, a noticeable dip around 3.3 eV suggests increased optical losses and reduced carrier collection at high photon energies. The enlarged view in Figure 5(d) highlights the relationship between the absorption edge, the metastable defect level located at $E_v$+0.92 eV, and the recombination processes occurring near the CdS/CISSe interface.

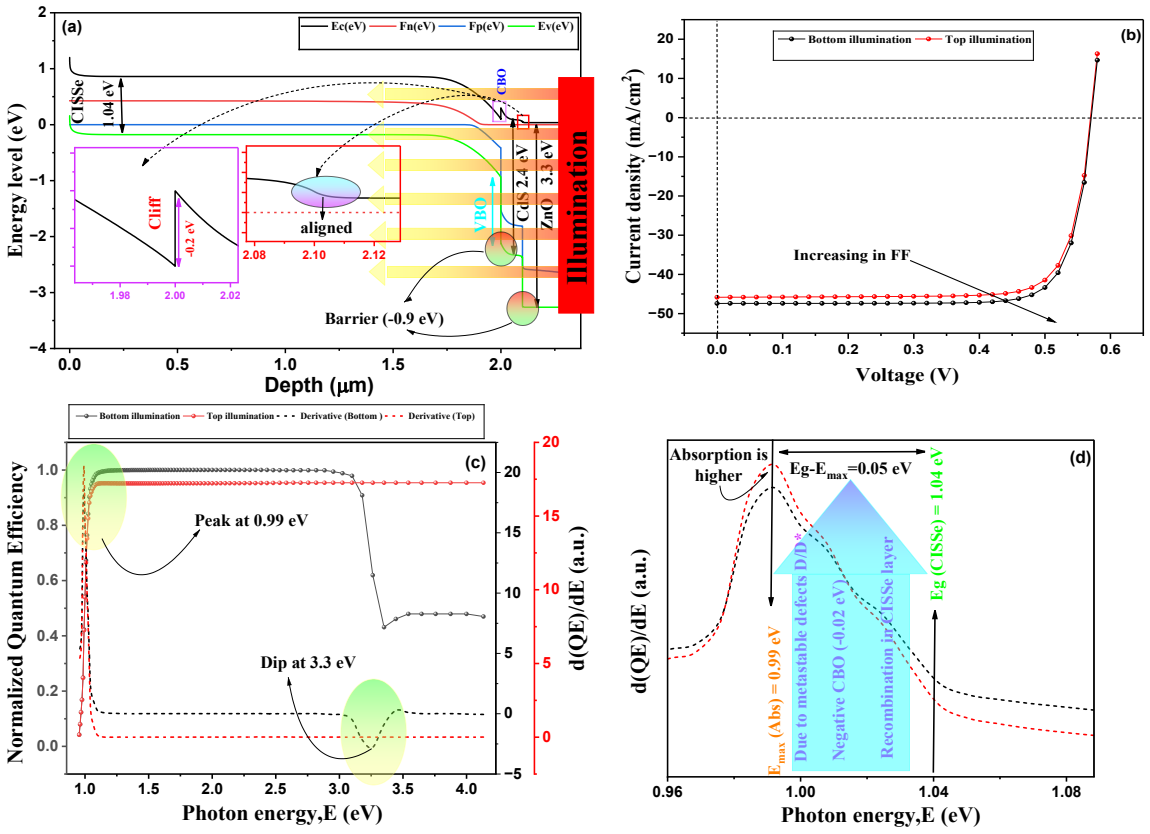



**Figure 05**. (a): energy diagram of CISSe based solar cell, (b): variation of (J-V) characteristic for top/bottom illumination, (c): variation of (QE) and its derivative with top and bottom illumination, (d): The zoomed section of (d (QE)/ dE).

### 3.2. Metal work function effect

Metal work function (MWF) is defined as the minimum energy required removing an electron from the surface [9]. Simulations were conducted using gold (Au), nickel (Ni), copper (Cu) graphite alloy, platinum (Pt) and niobium (Nb). The parameters for the contact materials used for the simulation are all based on the literature [28]. Figure 06 showed the effect of (MWF) on the solar cell efficiency. Higher MWF values reduced the barrier height for majority carriers, indicating that the contact approaches more Ohmic behavior. Thus, as (MWF) increased, the $V_{oc}$ and efficiency also increased. The highest efficiency (21 %) was achieved using Pt and Ni. Considering both cost and the performance of solar cell, the Ni was selected as the best back contact. This result is in good agreement with the data obtained by Atowar Rahman et al.[15]. Table 05 describes the influence of the metal work function (MWF) on the majority carrier barrier height at the metal/semiconductor contact. The behavior indicates a strong dependence of carrier transport on the contact energetics. As the metal work function increases from 4.9 to 5.7 eV, the majority carrier barrier height relative to the Fermi level ($E_f$) decreases from 0.24 to -0.36 eV. This reduction suggests an improvement in carrier extraction and a lower probability of carrier trapping by the metastable acceptor level located. A smaller barrier height facilitates the transport of majority carriers, which can enhance the electrical performance of the solar cell. Similarly, the majority carrier barrier height relative to $E_C/E_V$ decreases from 0.26 to -0.34 eV as the work function increases from 4.9 to 5.5 eV, confirming the reduction of the interfacial barrier. However, at higher work functions, the values become strongly shifted, indicating substantial band bending and modification of the band alignment at the interface.

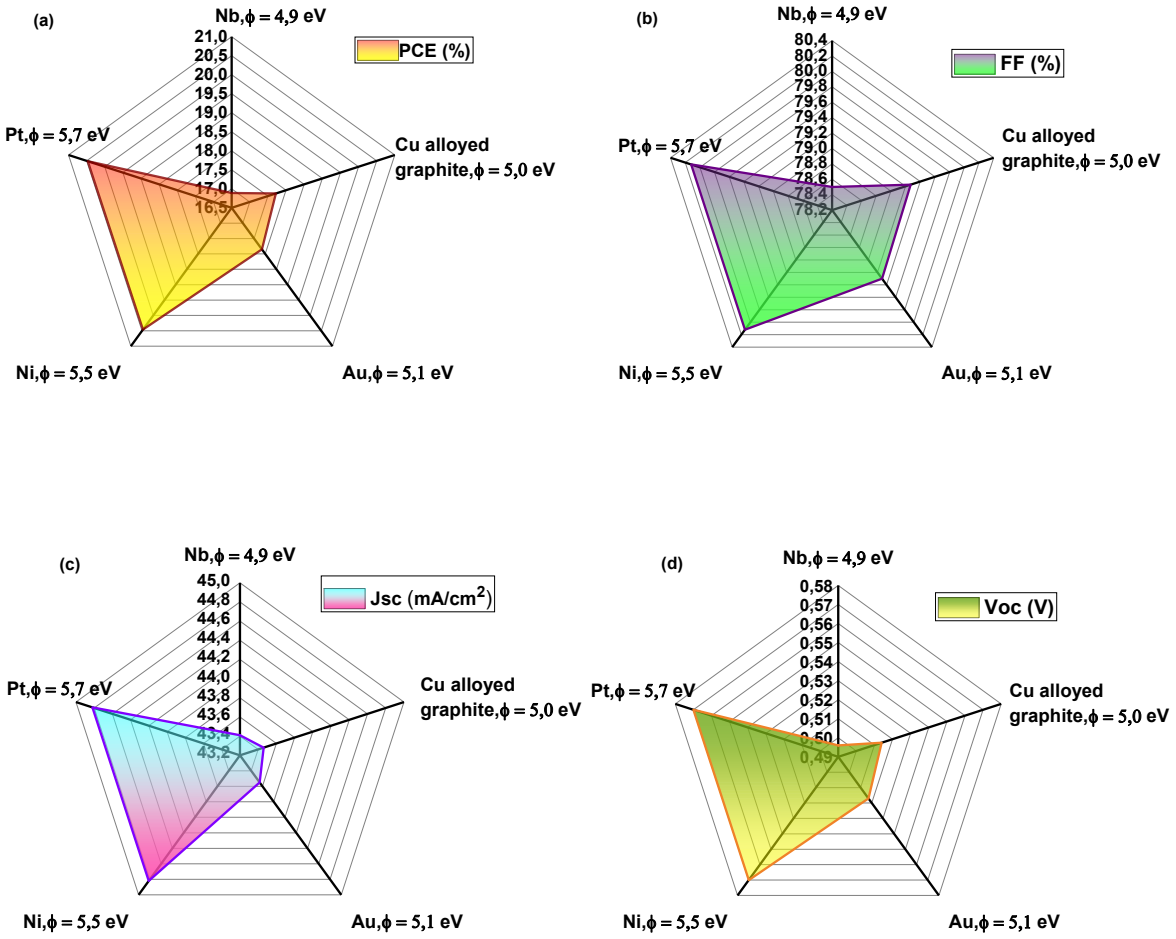



**Figure 06.** Plots of metal work function effect on photovoltaic parameters.

**Table 05.** Conduction/valence band energy between interfaces.

| Metal work function (MWF) | 4.9 | 5.0 | 5.1 | 5.5 | 5.7 |
|---|---|---|---|---|---|
| Majority carrier barrier height relative to: $E_f$ | 0.44 | 0.34 | 0.24 | -0.16 | -0.36 |
| Majority carrier barrier height relative to: Ec/Ev | 0.26 | 0.16 | 0.06 | -0.34 | 0.54 |

This interpretation is supported by the (J-V) characteristics shown in Figure 7(b), where the (J-V) curves exhibit a noticeable enhancement in fill factor compared with Nb, Cu-alloyed graphite, and Au. The power-voltage characteristics displayed in Figure 7(b) further confirm this trend. The maximum output power increases progressively from Nb to Pt, reaching its highest value for the high-work-function contacts. The improvement in ($P_{max}$) is directly associated with the simultaneous enhancement of $V_{oc}$, FF, and carrier collection efficiency.

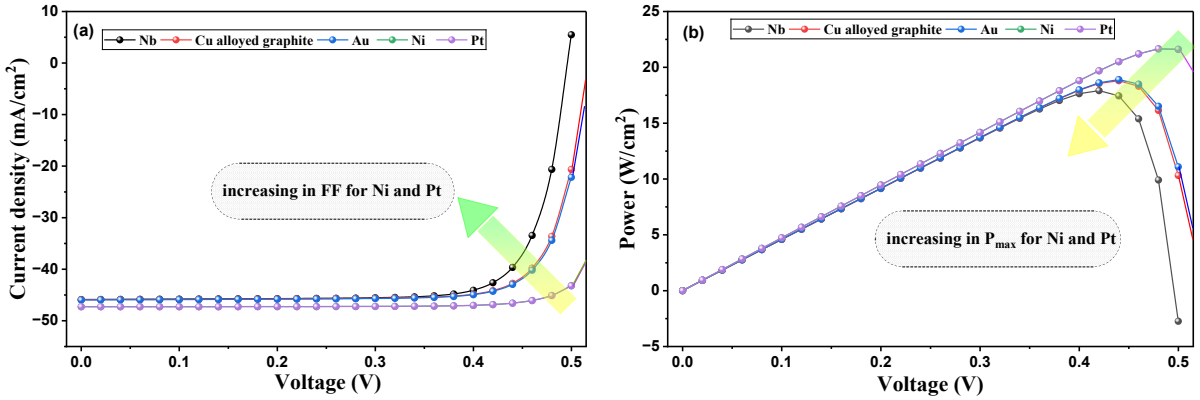



**Figure 07.** Plots of metal work function effect on photovoltaic parameters.

### 3.3. Rs and Rsh effect.

To investigate the effect of $R_s$ and $R_{sh}$ on CISSe/CdS/ZnO/SLG solar cell parameters, such as FF and efficiency, $R_s$ has been varied between 2 and 10 Ω.cm$^2$ and $R_{sh}$ has been varied from 0.1 to 10 KΩ.cm$^2$. Our results are illustrated in figure 08. The series resistance is due to the bulk resistance, the resistance of the metallic contacts of the front- and back surface and further circuit resistances from terminals and also from connections. The parallel resistance is caused by leakage currents. It is clear that the photovoltaic parameters are increasing with increasing of $R_{sh}$ and decreasing with increasing of Rs. This behavior can be explained by the increasing of leakage currents, which alter charge distribution and influence PV parameters [29]. When the Rs= 2 Ω.cm$^2$ and Rsh= 1 KΩ.cm$^2$ the solar cell exhibited FF =60.40 % and PCE=13.5 5% then they degrading significantly. This observation was deeply aligned with [20] and [30]. Using an equivalent circuit shown as a model of a solar cell (Figure 09) and including the Shockley diode (equation(1)) [31], we can deduce an equation (2) [31] which represents well the effects of resistive losses This equation is important for the understanding solar cells.

$$I = I_0\left(e^{\frac{Vj}{n\,V0}} - 1\right) \quad , \qquad I = I_L - I_0\left(e^{\frac{q(V+IRs)}{kT}} - 1\right) - \left(\frac{V+IRs}{Rsh}\right)$$

Where I is the current drawn from the cell, $I_0$ is the reverse saturation current, $V_j$ is the voltage the diode, $V_0$ is the thermal voltage, and n is the ideality factor. $I_L$ is the light induced current, Rs is the series resistance, k is the Boltzman constant, T is the temperature and q is the charge of the electron.

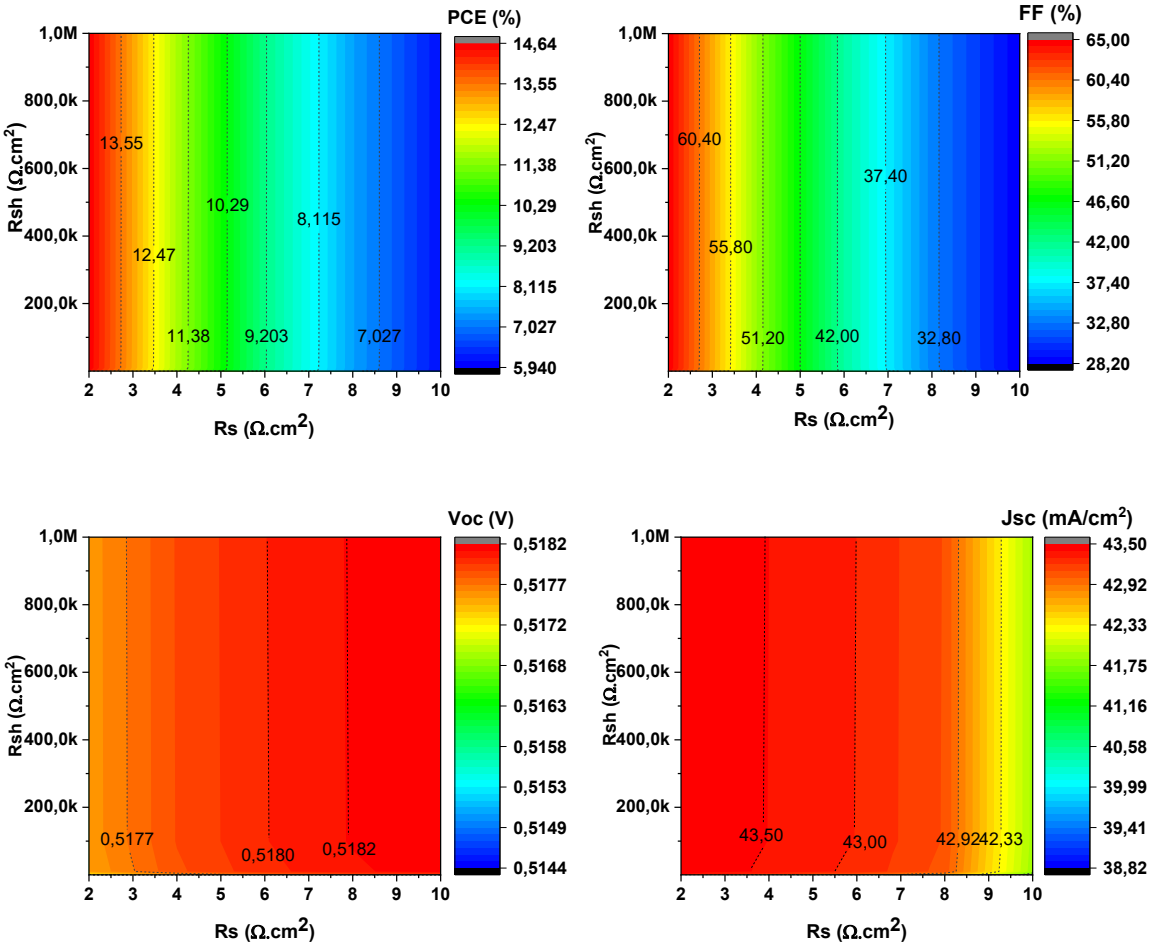



**Figure 08.** Contour mapping of $R_s/R_{sh}$ effect on photovoltaic parameters.

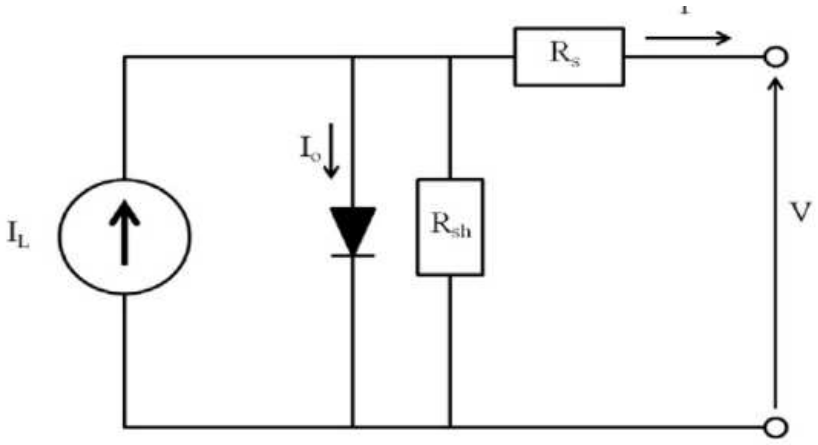



**Figure 09.** Equivalent circuit of CISSe based solar cell with $R_s/R_{sh}$.

### 3.4. Electron affinity (χ) and bandgap (Eg) effect.

The electron affinity and bandgap energy of the CISSe absorber layer play a decisive role in determining the band alignment at the buffer (CdS)/Absorber (CISSe) interface and, consequently, the charge-transport dynamics within the device [32]. By varying χ from 4.0 to 4.5 eV, the conduction-band offset (CBO) was modified from a blocking barrier to a small cliff. A moderate cliff (-0.1 to -0.2 eV) was found to enhance electron extraction while keeping interface recombination within acceptable limits. When electron affinity exceeded 4.3 eV, a large cliff formed, resulting in increased interfacial recombination and reduced $V_{oc}$ [16]. Similarly, tuning the CISSe bandgap from 1.0 to 1.5 eV revealed that photon absorption and carrier collection follow a competing trend: smaller bandgap values allow broader absorption but reduce $V_{oc}$, while larger bandgap values enhance $V_{oc}$ but decrease $J_{sc}$ due to reduced absorption of long-wavelength photons. The same observation was reported by [33].The figure 10 showed that the optimum performance was achieved near $E_g$ = 1.45 eV, which provided an excellent compromise between current generation and open-circuit voltage. At this optimal $E_g$, the device reached its highest simulated efficiency (33.34%) and FF (85.05 %), demonstrating the importance of band-gap engineering for high-performance CISSe solar cells. The improvement in photovoltaic performance observed at Eg=1.45 eV can be partially attributed to the reduction of recombination pathways associated with metastable defect states (D*).

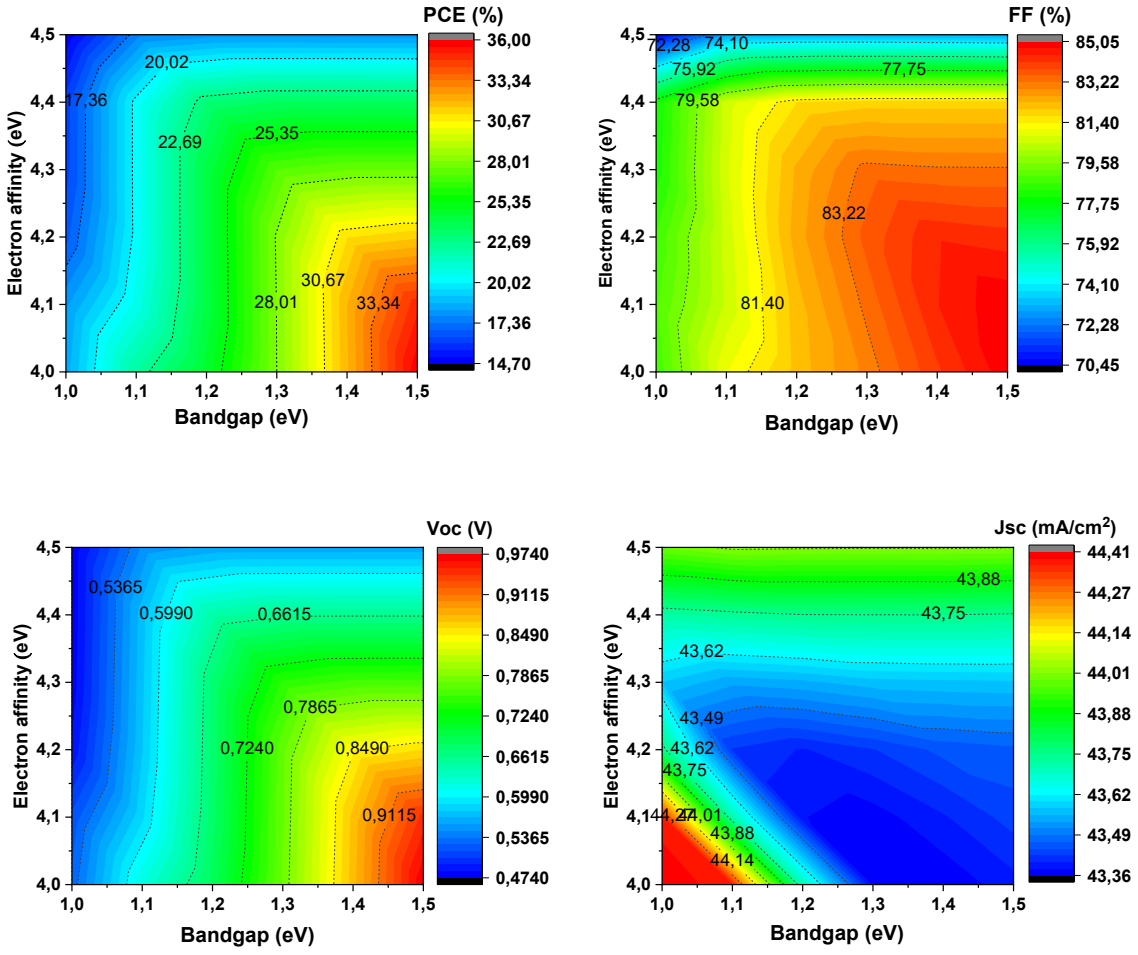



**Figure 10.** Contour mapping of $E_g$/χ effect on photovoltaic parameters.

**Funding declaration**

This research did not receive any specific grant from funding agencies in the public, commercial, or not-for-profit sectors.

**Data availability**

All data that support the findings of this study are included within this article.

**Conflicts of interest**

There are no conflicts to declare.

## Conclusion

In this work, a detailed SCAPS-1D simulation study of CISSe/CdS/ZnO/SLG thin-film solar cells was performed to investigate the combined effects of illumination direction, metal work function, parasitic resistances, electron affinity, and absorber bandgap on device performance under AM 1.5G illumination conditions. The obtained results demonstrated that photovoltaic performance is strongly controlled by interfacial band alignment, carrier transport dynamics, and electrical losses within the device structure. The comparative analysis between top and bottom illumination revealed that the conventional top-illuminated configuration achieved superior photovoltaic performance, with a PCE of 22.10%, fill factor of 80.31%, $V_{oc}$ of 0.5775 V, and $J_{sc}$ of 47.20 mA/cm². In contrast, bottom illumination resulted in a lower efficiency of 21.30% and FF of 79.70%, mainly due to increased recombination losses and less efficient carrier collection near the back interfaces. The band-alignment analysis further confirmed that the CdS/CISSe interface exhibits a cliff-like conduction-band offset of -0.2 eV, while the ZnO/CdS interface shows a large valence-band barrier of -0.9 eV, which can contribute to charge accumulation and interfacial recombination. The investigation of back-contact materials showed that increasing the metal work function from 4.9 to 5.7 eV significantly reduced the majority-carrier barrier height from 0.44 to -0.36 eV relative to the Fermi level, indicating a transition toward quasi-Ohmic contact behavior. As a result, both $V_{oc}$ and efficiency improved considerably, with Pt and Ni contacts providing the best photovoltaic response. The analysis also demonstrated that optimized resistive parameters are essential for minimizing electrical losses. The highest device performance was achieved at $R_s$ = 2 Ω.cm² and $R_{sh}$ = 10 K Ω.cm², confirming that low series resistance and high shunt resistance are critical for maintaining efficient carrier transport and suppressing leakage-current pathways. Furthermore, absorber-layer engineering revealed that the photovoltaic response strongly depends on the electronic structure of CISSe. By tuning the electron affinity from 4.0 to 4.5 eV and the bandgap from 1.0 to 1.5 eV, the conduction-band offset and carrier-collection mechanisms were effectively optimized. The optimum configuration was obtained at Eg = 1.45 eV and $\chi$ = 4.05 eV, leading to a maximum simulated efficiency of 33.34%, fill factor of 85.05%, $V_{oc}$ of 0.9115 V, and $J_{sc}$ of 44.27 mA/cm². These findings provide valuable physical insights and practical design strategies for the development of next-generation low-cost and high-efficiency photovoltaic technologies. Future studies may also explore alternative non-toxic buffer layers, two-dimensional passivation materials, and tandem-device architectures to further suppress recombination losses and enhance photovoltaic conversion efficiency beyond the limitations of conventional CISSe solar cells.

## References

[1] M. Atowar Rahman, “Enhancing the photovoltaic performance of Cd-free Cu2ZnSnS4 heterojunction solar cells using SnS HTL and TiO2 ETL,” *Sol. Energy*, vol. 215, pp. 64–76, Feb. 2021, doi: 10.1016/j.solener.2020.12.020.

[2] M. Abdelfatah, A. M. El Sayed, W. Ismail, S. Ulrich, V. Sittinger, and A. El-Shaer, “SCAPS simulation of novel inorganic ZrS2/CuO heterojunction solar cells,” *Sci. Rep.*, vol. 13, no. 1, p. 4553, Mar. 2023, doi: 10.1038/s41598-023-31553-4.

[3] S. A. Moiz, A. N. M. Alahmadi, and A. J. Aljohani, “Design of a Novel Lead-Free Perovskite Solar Cell for 17.83% Efficiency,” *IEEE Access*, vol. 9, pp. 54254–54263, 2021, doi: 10.1109/ACCESS.2021.3070112.

[4] S. E. Lachhab, A. Bliya, E. A. Ibrahmi, and L. Dlimi, “Improvement of CISSe / CdS / ZnO Structure Performance by SCAPS-1D.,” Oct. 19, 2021, *In Review*. doi: 10.21203/rs.3.rs-965170/v1.
[5] K. Kushiya, “CIS-based thin-film PV technology in solar frontier K.K.,” *Sol. Energy Mater. Sol. Cells*, vol. 122, pp. 309–313, Mar. 2014, doi: 10.1016/j.solmat.2013.09.014.
[6] M. A. Ghebouli, B. Ghebouli, R. Larbi, T. Chihi, and M. Fatmi, “Effect of buffer nature, absorber layer thickness and temperature on the performance of CISSe based solar cells, using SCAPS-1D simulation program,” *Optik*, vol. 241, p. 166203, Sep. 2021, doi: 10.1016/j.ijleo.2020.166203.
[7] C. Deline, D. Jordan, B. Sekulic, J. Parker, B. McDanold, and A. Anderberg, “PV Lifetime Project - 2024 NREL Annual Report,” *Renew. Energy*, 2024.
[8] M. Isah *et al.*, “Exploring the impact of defect energy levels in CdTe/Si dual-junction solar cells using wxAMPS,” *Sci. Rep.*, vol. 14, no. 1, p. 4804, Feb. 2024, doi: 10.1038/s41598-024-55616-2.
[9] M. Chettab *et al.*, “Influence of Physical Parameters on p-CuO/n-CdS/n-Zn2SnO4 Solar cell: A Numerical Investigation Achieving Efficiency of 28.50 % Using SCAPS-1D,” 2026.
[10] S. Rabhi, H. Benzouid, A. Slami, and K. Dadda, “Modeling and Numerical Simulation of a CH3NH3SnI3 Perovskite Solar Cell Using the SCAPS1-D Simulator,” in *ASEC 2023*, MDPI, Oct. 2023, p. 97. doi: 10.3390/ASEC2023-15300.
[11] A. Umar *et al.*, “Modeling and Simulation of Tin Sulfide (SnS)-Based Solar Cell Using ZnO as Transparent Conductive Oxide (TCO) and NiO as Hole Transport Layer (HTL),” *Micromachines*, vol. 13, Nov. 2022, doi: 10.3390/mi13122073.
[12] A. Mortadi, E. El Hafidi, H. Nasrellah, M. Monkade, and R. El Moznine, “Analysis and optimization of lead-free perovskite solar cells: investigating performance and electrical characteristics,” *Mater. Renew. Sustain. Energy*, vol. 13, no. 2, pp. 219–232, Aug. 2024, doi: 10.1007/s40243-024-00260-z.
[13] J. Xia, “Optimizing CZTSSe solar cell performance through engineered $TiO_2$ bandgap: quantitative insights from SCAPS-1D device simulation,” *Phys. Scr.*, vol. 100, no. 9, p. 095004, Sep. 2025, doi: 10.1088/1402-4896/adfe2f.
[14] T. Minemoto *et al.*, “Control of conduction band offset in wide-gap Cu(In,Ga)Se solar cells,” *Sol. Energy Mater. Sol. Cells*, vol. 75, no. 1–2, pp. 121–126, Jan. 2003, doi: 10.1016/S0927-0248(02)00120-4.
[15] M. A. Rahman, “Design and simulation of a high-performance Cd-free Cu2SnSe3 solar cells with SnS electron-blocking hole transport layer and TiO2 electron transport layer by SCAPS-1D,” *SN Appl. Sci.*, vol. 3, no. 2, p. 253, Feb. 2021, doi: 10.1007/s42452-021-04267-3.
[16] M. Sood *et al.*, “Origin of Interface Limitation in Zn(O,S)/$CuInS_2$ -Based Solar Cells,” *ACS Appl. Mater. Interfaces*, vol. 14, no. 7, pp. 9676–9684, Feb. 2022, doi: 10.1021/acsami.1c19156.
[17] M. Noman, A. H. H. Khan, and S. T. Jan, “Interface engineering and defect passivation for enhanced hole extraction, ion migration, and optimal charge dynamics in both lead-based and lead-free perovskite solar cells,” *Sci. Rep.*, vol. 14, no. 1, p. 5449, Mar. 2024, doi: 10.1038/s41598-024-56246-4.
[18] M. Burgelman, P. Nollet, and S. Degrave, “Modelling polycrystalline semiconductor solar cells,” *Thin Solid Films*, vol. 361–362, pp. 527–532, Feb. 2000, doi: 10.1016/S0040-6090(99)00825-1.
[19] J. Al Mahmud *et al.*, “Design and analysis of a $SnS_2$ /$WS_2$ /$V_2$ $O_5$ double-heterojunction toward high-performance photovoltaics,” *Energy Adv.*, vol. 2, no. 11, pp. 1843–1858, 2023, doi: 10.1039/D3YA00231D.
[20] M. Hossain *et al.*, “Combined DFT, SCAPS-1D, and wxAMPS frameworks for design optimization of efficient Cs2BiAgI6-based perovskite solar cells with different charge transport layers,” *RSC Adv.*, vol. 12, pp. 34850–34873, Dec. 2022, doi: 10.1039/d2ra06734j.
[21] J. C. Z. Medina *et al.*, “Numerical Simulation and Performance Optimization of a Solar Cell Based on WO3/CdTe Heterostructure Using NiO as HTL Layer by SCAPS 1D,” *Coatings*, vol. 13, no. 8, p. 1436, Aug. 2023, doi: 10.3390/coatings13081436.
[22] M. U. Salman and S. Atiq, “Analysis of short-circuit current suppression mediated by strategically optimized buffer layer thickness in heterojunction solar cells,” *Energy Adv.*, vol. 4, no. 12, pp. 1500–1509, 2025, doi: 10.1039/D5YA00290G.
[23] F. Belarbi, W. Rahal, D. Rached, S. Benghabrit, and M. Adnane, “A comparative study of different buffer layers for CZTS solar cell using Scaps-1D simulation program,” *Optik*, vol. 216, p. 164743, Aug. 2020, doi: 10.1016/j.ijleo.2020.164743.
[24] M. K. Hossain *et al.*, “Deep Insights into the Coupled Optoelectronic and Photovoltaic Analysis of Lead-Free $CsSnI_3$ Perovskite-Based Solar Cell Using DFT Calculations and SCAPS-1D Simulations,” *ACS Omega*, vol. 8, no. 25, pp. 22466–22485, Jun. 2023, doi: 10.1021/acsomega.3c00306.
[25] B. Salhi, “The Photovoltaic Cell Based on CIGS: Principles and Technologies,” *Materials*, vol. 15, no. 5, p. 1908, Mar. 2022, doi: 10.3390/ma15051908.
[26] M. Sood *et al.*, “Electrical barriers and their elimination by tuning (Zn,Mg)O composition in Cu(In,Ga)S2: Systematic approach to achieve over 14% power conversion efficiency”.
[27] T. Wu *et al.*, “Heterogeneous FASnI3 Absorber with Enhanced Electric Field for High-Performance Lead-Free Perovskite Solar Cells,” *Nano-Micro Lett.*, vol. 14, no. 1, p. 99, Dec. 2022, doi: 10.1007/s40820-022-00842-4.
[28] P. Sawicka-Chudy *et al.*, “Simulation of $TiO_2$ /CuO solar cells with SCAPS-1D software,” *Mater. Res. Express*, vol. 6, no. 8, p. 085918, Jun. 2019, doi: 10.1088/2053-1591/ab22aa.

[29] K. Jenifer, B. Gururajan, W. Liu, and S. Parthiban, “Numerical Investigation of Eco-Friendly All-Zinc Based Thin Film Solar Cells For Sustainable Photovoltaics,” *Adv. Theory Simul.*, vol. 8, no. 11, p. e00157, Nov. 2025, doi: 10.1002/adts.202500157.
[30] Z. Younsi *et al.*, “Mitigating the interface defects influence on SnSe solar cells using optimized electron transport layer,” *Discov. Mater.*, vol. 4, no. 1, p. 85, Dec. 2024, doi: 10.1007/s43939-024-00156-9.
[31] H. Heriche, Z. Rouabah, and N. Bouarissa, “New ultra thin CIGS structure solar cells using SCAPS simulation program,” *Int. J. Hydrog. Energy*, vol. 42, no. 15, pp. 9524–9532, Apr. 2017, doi: 10.1016/j.ijhydene.2017.02.099.
[32] T. A. Chowdhury, “Numerical modeling to enhance the efficiency of experimentally fabricated $Sb_2$ $Se_3$ -based solar cell,” *RSC Adv.*, vol. 16, no. 3, pp. 2873–2903, 2026, doi: 10.1039/D5RA04411A.
[33] P. Afrin, K. Farjana, A. Vumije, and Md. N. Uddin, “An investigation on the impact of temperature variation over the performance of formamidinium tin iodide perovskite solar cell using SCAPS simulation,” *AIP Adv.*, vol. 14, no. 7, p. 075123, Jul. 2024, doi: 10.1063/5.0209332.